Chapter 2

Optics for Diffuse Photon Density Waves

In order to develop models for the forward and inverse problems, we must first understand how photons travel through homogeneous media. In this section we begin by describing the passage of photons through homogeneous media, and later incorporate heterogeneous media using planar and curved boundaries. In this work we treat the photons as particles, ignoring polarization and interference effects. This approach is valid when the mean free path for photon scattering ($1/\mu_s'$) is much smaller than the absorption length ($1/\mu_a$) and much smaller than the sample size. The optical properties of some human tissues (table 2.1) demonstrate that this approximation is good for systems such as the brain or breast, and source detector separations of a few random walk steps.

As light enters such a medium, the photons undergo a random walk. When the source-detector separation is much greater than the random walk mean free path, the photon propagation can be modeled by the diffusion approximation to the Boltzmann transport equation [3].

$$\frac{\partial U(\mathbf{r},t)}{\partial t} + v\mu_a U(\mathbf{r},t) + \nabla \cdot \mathbf{J}(\mathbf{r},t) = q_o(\mathbf{r},t), \tag{2.1}$$

$$\nabla U(\mathbf{r},t) + \frac{3\partial \mathbf{J}(\mathbf{r},t)}{v^2 \partial t} + \frac{\mathbf{J}(\mathbf{r},t)}{D} = 0 \tag{2.2}$$

where U is the photon density (number of photons per unit volume), $\mathbf{J}$ is the photon current density (number of photons per unit area per unit time), q_o is the isotropic source term (number of photons per unit volume per unit time), v is the speed of

Tissue Type	Optical Wavelength (nm)	μ_a (cm^{-1})	μ_s' (cm^{-1})	Test
Human Back - normal	811	0.09	10.5	1
Human Back - tumor	811	0.20	9.5	1
Human Abdomen - normal	811	0.09	9.5	1
Human Abdomen - tumor	811	0.20	8.0	1
Breast, glandular	700	0.5	14	2
Breast, adipose	700	0.7	9	2
Breast, fibrocystic	700	0.2	13	2
Breast, fibrodema	700	0.5	7	2
Breast, ductal carcinoma	700	0.5	12	2
White Matter	633	0.22	9.1	3
Grey Matter	633	0.27	20.6	3
Whole Blood, oxygenated	665	1.30	6.11	4
Whole Blood, partially oxygenated	630	14.3	8.9	5

Test descriptions

(1) In vivo, frequency scanning device. See [34] (2) Frozen sections, thawed; 1 mm slabs for (R,T) single integrating sphere with monochromator for R and T;2-polarizers to filter scattered axial light for direct T.(3) Freshly resected slabs, integrating sphere. (4) diluted, heparinized,in cuvettes; absorbence+goniometry. (5) Freshly drawn, heparinized (anti-clotting agent added), oxygenated at atmospheric equilibrium; semi-infinite slab (Rd); thin cuvettes diffuse R of whole blood;direct T of diluted blood, hemolyzed RBC's, and centrifuge-isolated plasma.

Table 2.1: The optical properties of human tissues.
Downloaded from ftp://laser.mda.uth.tmc.edu/pub/

light in the medium, μ_a is the absorption coefficient, D is the diffusion coefficient,

$$D = \frac{v}{3\mu_s'}, \tag{2.3}$$

and μ_s' is the reduced scattering coefficient. The scattering coefficient μ_s is the reciprocal of the scattering length. The reduced scattering coefficient is the reciprocal of the random walk step, i.e. the average length it takes for a photon's direction to become random. The scattering coefficient and the reduced scattering coefficient are related by the single-scattering anisotropy factor, g, a measure of how much of the incident light is scattered in the forward direction. Specifically, it is the average of the cosine of the *single-scattering* scattering angle.

$$\mu_s' = \mu_s(1-g) = \mu_s(1- < \cos\theta >) \tag{2.4}$$

In typical biological tissues, the scattering is predominately in the forward direction (g = 0.9). For example, in breast tissue, the scattering length is about 0.1 mm, but the random walk step is 1 mm, that is it takes about 10 scattering events for the photon direction to become random with respect to its incident direction.

If the source is an amplitude modulated point source of the form,

$$q_o(\mathbf{r},t) = \delta(\mathbf{r})\{A + Be^{-i\omega t}\}, \tag{2.5}$$

then our solutions U and $\mathbf{J}$ will have ac and dc parts i.e.

$$U(\mathbf{r},t) = U_{dc}(\mathbf{r}) + U_{ac}(\mathbf{r})e^{-i\omega t}, \tag{2.6}$$

$$\mathbf{J}(\mathbf{r},t) = \mathbf{J}_{dc}(\mathbf{r}) + \mathbf{J}_{ac}(\mathbf{r})e^{-i\omega t}. \tag{2.7}$$

The differential equations for the dc parts are:

$$v\mu_a U_{dc}(\mathbf{r}) + \nabla\cdot\mathbf{J}_{dc}(\mathbf{r}) = A\delta(\mathbf{r}), \tag{2.8}$$

$$\nabla U_{dc}(\mathbf{r}) + \frac{\mathbf{J}_{dc}(\mathbf{r})}{D} = 0 \tag{2.9}$$

so

$$v\mu_a U_{dc}(\mathbf{r}) - \nabla\cdot(D\nabla U_{dc}(\mathbf{r})) = A\delta(\mathbf{r}) \tag{2.10}$$

$$v\mu_a U_{dc}(\mathbf{r}) - D\nabla^2 U_{dc}(\mathbf{r}) = A\delta(\mathbf{r}). \tag{2.11}$$

Here we have used the fact the D is homogeneous so $\nabla D = 0$. The general solution for U is a superposition of the two spherical wave solutions,

$$U_{dc} = C_1 \frac{e^{-kr}}{4\pi D r} + C_2 \frac{e^{kr}}{4\pi D r}, \tag{2.12}$$

$$k = \sqrt{\frac{v\mu_a}{D}}, \tag{2.13}$$

The constant C_2 must be zero to satisfy the boundary condition that $U_{dc} = 0$ at infinity. When we plug the particular solution into the Helmholtz equation we see that $C_1 = A/D$.

In this work we are generally most interested in the ac components of equation 2.1 and 2.2:,

$$-i\omega U_{ac}(\mathbf{r}) + v\mu_a U_{ac}(\mathbf{r}) + \nabla \cdot \mathbf{J}_{ac}(\mathbf{r}) = B\delta(\mathbf{r}), \tag{2.14}$$

$$\nabla U_{ac}(\mathbf{r}) + \frac{-3i\omega \mathbf{J}_{ac}(\mathbf{r})}{v^2} + \frac{\mathbf{J}_{ac}(\mathbf{r})}{D} = 0 \tag{2.15}$$

Thus,

$$\mathbf{J}_{ac}(\mathbf{r}) = \frac{-D}{1 - 3i\omega D/v^2} \nabla U_{ac}(\mathbf{r}). \tag{2.16}$$

For most biological tissues of interest,

$$1 >> 3\omega D/v^2 \quad . \tag{2.17}$$

For example, for breast tissue, $D \approx 10^9\ m^2/s$, and we typically use $\omega \approx 5 \times 10^8\ s^{-1}$ so $3\omega D/v^2 \approx 0.002$. So

$$\mathbf{J}_{ac}(\mathbf{r}) \approx -D\nabla U_{ac}(\mathbf{r}). \tag{2.18}$$

We now plug equation 2.18 into 2.14,

$$-D\nabla^2 U_{ac}(\mathbf{r}) + (-i\omega + v\mu_a)U(\mathbf{r}) = B\delta(\mathbf{r}), \tag{2.19}$$

$$(\nabla^2 + k^2)U(\mathbf{r}) = -B\delta(\mathbf{r})/D. \tag{2.20}$$

Again, we have used the fact that D is homogeneous. The particular ac solution to this Helmholtz Equation in an infinite medium is

$$U(\mathbf{r}) \equiv U_{ac}(\mathbf{r}) = \frac{-B}{D} \frac{e^{ikr}}{4\pi r} \tag{2.21}$$

where

$$k^2 = (-v\mu_a + i\omega)/D, \tag{2.22}$$

$$k = \Re(k) + i\Im(k) \tag{2.23}$$

$$Real\ part: \quad \Re(k) = \left(\frac{v^2\mu_a^2 + \omega^2}{D}\right)^{1/4} \sin\left(\frac{1}{2}tan^{-1}\left(\frac{\omega}{v\mu_a}\right)\right) \tag{2.24}$$

$$Imaginary: \quad part\ \Im(k) = \left(\frac{v^2\mu_a^2 + \omega^2}{D}\right)^{1/4} \cos\left(\frac{1}{2}tan^{-1}\left(\frac{\omega}{v\mu_a}\right)\right). \tag{2.25}$$

Thus, a damped, scalar, spherical wave of light energy density is generated by the source at the origin. The wave has a well defined amplitude and phase at each position, **r**.

In this section we will experimentally demonstrate that a great deal of traditional optics can be applied to DPDW's - albeit in the near field. For example, we will show that these waves interfere and refract. Other work from our lab has demonstrated that DPDW's diffract and scatter from heterogeneities [7]. The mathematics is slightly different from electromagnetic optics, because the disturbance is a scalar wave, i.e.

$$EM\ wave: \ \vec{E} = \vec{E}_o \frac{e^{i\vec{k}\cdot\vec{r}}}{4\pi|\vec{r}|} \qquad DPDW: \ U = A_o \frac{e^{ik|\vec{r}|}}{4\pi|\vec{r}|}. \tag{2.26}$$

The fact that we have a scalar wave implies fewer degrees of freedom for the wave, and less complex boundary conditions. This generally simplifies the calculations. It is interesting that because the wavelength is on the order of 10 cm, and we make measurements with typical source-detector separations of 6 cm, we are making near field measurements. This means that the conventional ideas about resolution, which were derived from the far-field approximation, do not apply. For instance, the Rayleigh criteria for fundamental resolution limits states that two objects cannot be resolved if they are within $\lambda/2$ of each other. This is not true for diffusive imaging. In fact, we have shown through experiment that one can clearly resolve two objects which are separated by a distance of less than $\lambda/4$ (see figure 4.14). In diffusive imaging the fundamental resolution limit is the graininess of the theory, the random walk step governing diffusion theory. In practice, the resolution and characterization limits are determined by signal to noise considerations [22].

We begin by demonstrating that these waves exist in a homogeneous, infinite medium. Our experimental setup consisted of a large fish tank (30 x 30 x 60 cm) filled with a model biological material called Intralipid [35]. Intralipid is a turbid, polydisperse suspension of soy lipid. The particle diameter ranges from about 0.1μm to 1.1μm with an average of about 0.4μm. By changing the solution concentration one can vary the light diffusion constant over a wide range. We typically use concentrations varying from 0.1% (D = $7.5 \times 10^9 m^2/s$) to 1.5% (D = $5.0 \times 10^9 m^2/s$). We can also add inks (such as india ink) and dyes (such as any water soluble laser dye) to vary the absorption coefficient. The absorption of the inks and dyes can be calibrated in a standard spectrophotometer. A laser diode was fiber coupled to the medium using a 0.3 cm diameter fiber bundle, and a similar optical fiber was used to detect diffuse photons. A translation stage enabled measurements of amplitude and phase as a function of position within the tank.

The experimental setup is described in detail in chapter 3. Briefly, source and detector optical fibers ($\approx$3 mm in diameter) were immersed in the solution at the same height above the tank floor (see figure 2.1). The source light was derived from a 3 mW diode laser operating at 780 nm. The diode laser was amplitude modulated at 200 MHz. The detector fiber could be positioned anywhere in the plane, and was connected to a photomultiplier tube on its other end. In order to facilitate the phase and amplitude measurements, both the reference signal from the source and the detected signal were down-converted to 25 kHz by heterodyning with a second oscillator at 200.025 MHz. The low frequency signals were then measured using a lock-in amplifier. The phase shift and AC amplitude of the detected light were measured with respect to the source at each point on a 0.5 cm square planar grid throughout the sample. Constant phase contours were easily determined by linear interpolation of the grid data. Since the signal amplitude decays by a factor of $e^{2\pi}/r$ in one wavelength, the range of our experiments is limited to slightly more than one wavelength. Nevertheless it is possible to clearly distinguish the essential physical phenomena in the experiments.

Throughout this work, we assume that we have an isotropic point source and a point detector. In reality, we have a finite detector area (usually about 3 mm diameter) and a nearly collimated source fiber with a finite size (usually 1-3 mm diameter). In a collimnated source, the light will travel ballistically for approximately one random walk step. After 1 random walk step, a significant portion of the light has been scattered, and the isotropic source approximation is a good approximation. Some researchers place an effective source one random walk step away from the true source to correct for this effect. In this work we have not investigated or used a correction method. This will contribute small errors in the experimental measurements.

Figure 2.1 shows the measured constant phase contours of the disturbance produced by a fiber source located at the origin. First we note that the phase contours are spherical and centered about the source position. Second, both the phase and the log of the amplitude times the source-detector separation are linear with the source-detection separation as shown in the inset of figure 2.1. We can calculate the absorption and scattering coefficients of the medium from the measurements of amplitude and phase. Typically, we characterize a medium by measuring the amplitude and phase as a function of distance. The slopes of these lines give us the real and imaginary parts of the wavenumber k;

$$ln(r|U(\mathbf{r})|) = -\Im(k)r + ln(B) - ln(4\pi D) \ , \tag{2.27}$$

$$phase(U(\mathbf{r})) = \Re(k)r \ . \tag{2.28}$$

Once we know k, we can easily calculate the absorption and and reduced scattering of the medium,

$$1/\mu_a = \frac{v}{\omega} tan\left(2 \ tan^{-1}\left(\frac{\Re(k)}{\Im(k)}\right)\right) \tag{2.29}$$

$$1/D = \frac{\Re(k)^2 + \Im(k)^2}{(v^2\mu_a^2 + \omega^2)^{1/2}} \ . \tag{2.30}$$

From these measurements we deduced the wavelength of the diffuse photon density wave (11.2 cm), as well as the photon transport mean free path (0.1 cm), and the

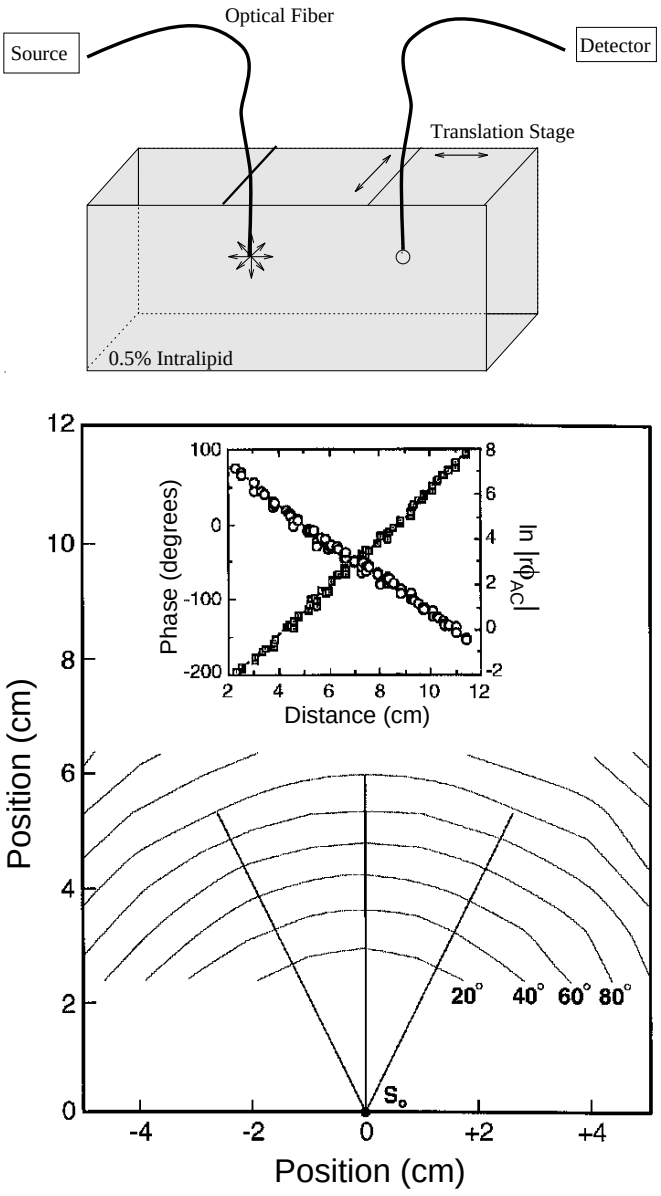

Figure 2.1: Constant phase contours shown as a function of position for homogeneous, 0.5% Intralipid solution. The contours are shown in 20 degree intervals. Inset: The measured phase shift (circles), and $ln(rU_{ac}(r))$ (squares) are plotted as a function of radial distance from the source S_o.

photon absorption length (52.4 cm) in 0.5% Intralipid at room temperature. The photon absorption can be attributed almost entirely to water [36] at 780 nm.

In figure 2.2 we demonstrate the refraction of these waves in three ways. Figure 2.2 shows constant phase contours (every 20°). This time however, a plane boundary was introduced, separating the lower medium with concentration $[l] = 1.0\%$ and light diffusion coefficient D_l, from the upper medium with concentration $[u] = 0.25\%$ and light diffusion coefficient D_u. The contours below the boundary are just the homogeneous media contours (without reflection); they were obtained before the partition was introduced into the sample. The contours above the boundary were derived from the diffuse photon density waves transmitted into the less concentrated medium. As a result of our detector geometry, our closest approach to the partition was about 1 cm. We expect a number of general results. First, the wavelength in the less dense medium ($\lambda_u = 14.8$ cm) should be greater than the wavelength of the diffuse photon density wave in the incident medium ($\lambda_l = 8.17$ cm). This was observed. The ratio of the two wavelengths should equal the ratio of the diffusive indices of refraction of the two media. Specifically we found, as expected, that

$$\lambda_u = \lambda_l \sqrt{\frac{D_l}{D_u}} \approx \lambda_l \sqrt{\frac{[l]}{[u]}}. \tag{2.31}$$

We would expect that the apparent source position (S_i), as viewed from within the upper medium, should be shifted from the real source position ($S_o = 4.0 \pm 0.2$ cm) by the factor λ_l / $\lambda_u = 0.55$. Using the the radii from the full contour plots, we see that the apparent source position is shifted from 4.0 ± 0.2 cm to 2.0 ± 0.25 cm.

Finally in figure 2.2 we explicitly demonstrate Snell's law for diffuse photon density waves. This can be seen by following the ray from S_o to the point A at the boundary, and then into the upper medium. The ray in the lower medium makes an angle $\theta_i = 14°$ with respect to the surface normal. The upper ray is constructed in the standard way between the apparent source position S_i, through the point A on the boundary, and into the medium above the boundary [37]. It is perpendicular to the circular wavefronts in the less dense medium, and makes an angle $\theta_t = 26.6°$ with respect to

the boundary normal. Within the accuracy of the experiment we see that

$$\frac{\sin(\theta_i)}{\sin(\theta_t)} = 0.54 \approx \frac{\lambda_l}{\lambda_u} \ , \tag{2.32}$$

Thus Snell's law accurately describes the propagation of diffuse photon density waves across the boundary. It is interesting to note that the wavefronts become quite distorted when the source ray angle exceeds 30° . These irregularities are a consequence of total internal reflection, diffraction, and some spurious boundary effects.

A third important observation is presented in figure 2.3. We used a circular boundary separating two turbid media to demonstrate that we can alter the curvature of the diffuse photon density wavefronts in analogy with a simple lens in optics. The constant phase contours on the left occur in 20° intervals, and the constant phase contours on the right occur in 40° intervals. The constant phase contours of the transmitted wave exhibit a shorter wavelength, and are clearly converging toward some image point to the right of the boundary. The medium on the left (l_l) has an Intralipid concentration of $[l] \approx 0.1\%$, and the medium on the right (l_r) has a concentration of $[r] \approx 1.6\%$. The wavelength ratio was measured to be $l_r/l_l = 3.8 \pm 0.3$. The curved surface has a radius R = 9.0 ± 0.4 cm. The object position (the source) is $S_o = 9.4 \pm 0.3$ cm, and the image position $S_i = 10.9$ cm is predicted from the well known paraxial result from geometrical optics for imaging by a spherical refracting surface [37];

$$\frac{\sqrt{1/[l]}}{S_o} + \frac{\sqrt{1/[r]}}{S_i} = \frac{\sqrt{1/[r]} - \sqrt{1/[l]}}{R} \tag{2.33}$$

The image position was measured to be $S_i = 12 \pm 2$ cm, which is close to the predicted value, 10.9 cm. The image position was found by using a compass to determine the center of the four wavefronts. Although the error in this measurement is large, the central point remains, that is, the curvature of the wavefronts is reversed after traversing the circular boundary.

DPDW's have also been shown to interfere. In much of our work, we will exploit the destructive interference of two DPDW's to increase our sensitivity to heterogeneities [9] and reduce our sensitivity to the background properties. In a typical

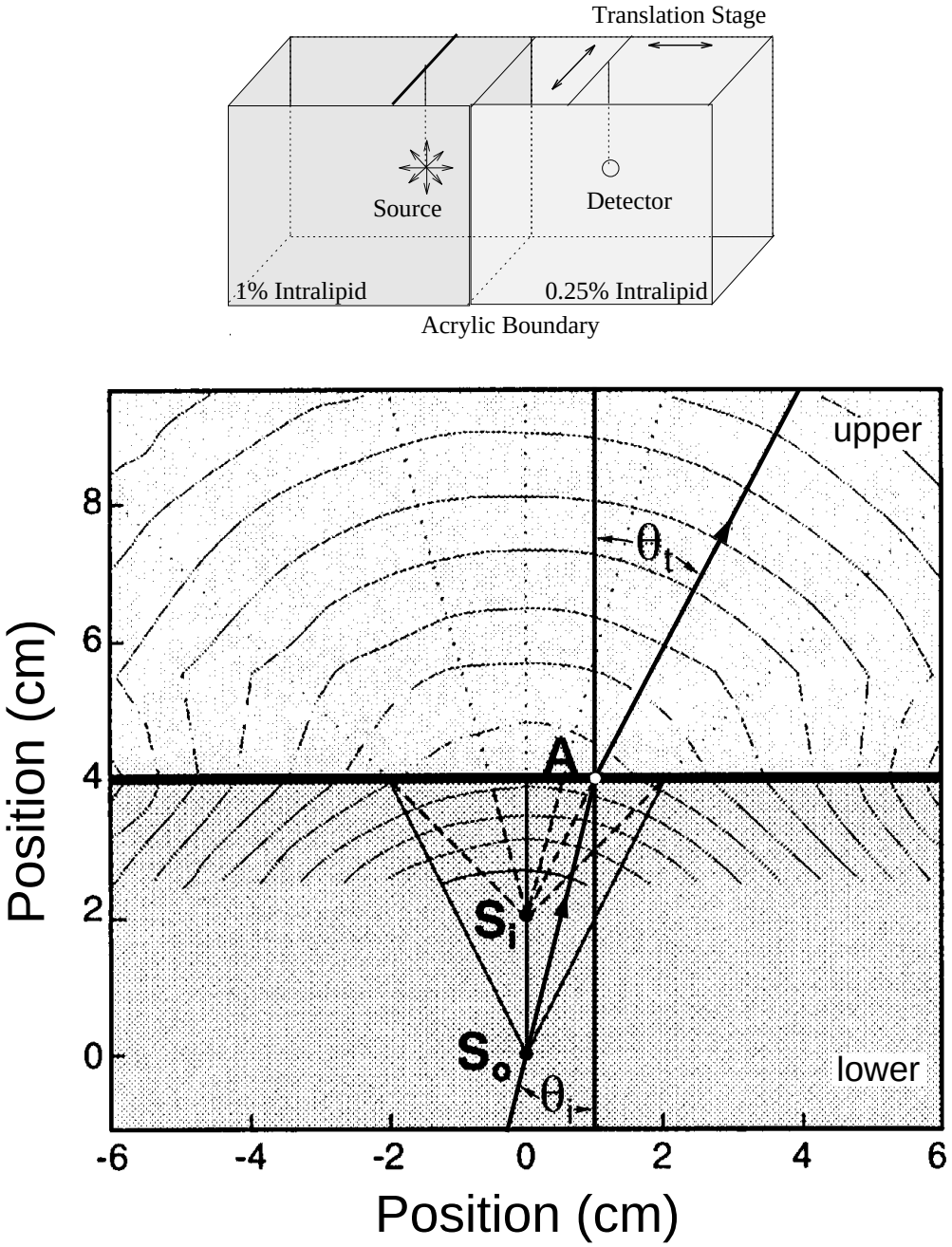

Figure 2.2: Constant phase contours (in 20 degree intervals) as a function of position showing the propagation of a diffuse photon density wave across a planar boundary. The solid lines are obtained directly from data. The dot-dashed lines are obtained by interpolation over large distances, and are drawn to show the irregularities at large angles.

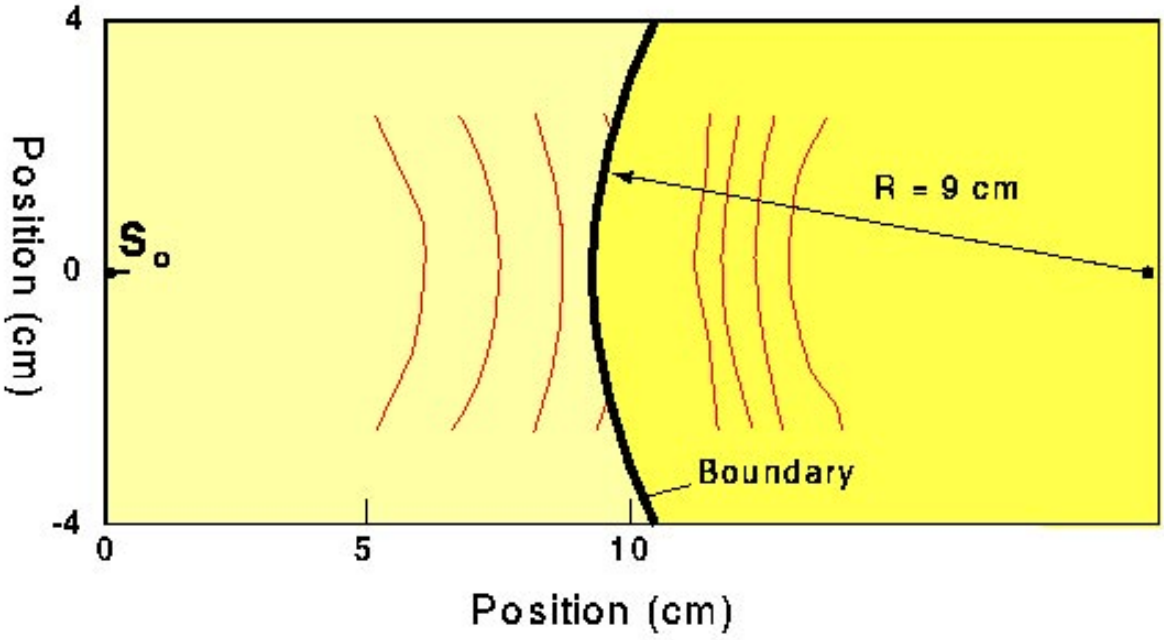

Figure 2.3: Refraction by a spherical surface. The reversal of wavefront curvature is evident.

configuration, we use two spatially separated sources, 180° out of phase with each other. The amplitude and phase of such a superposition are shown in figure 2.4. Note that at points equidistant from the two sources, the waves interfere destructively causing an amplitude null and a sharp 180° phase shift in the DPDW. If a detector is scanned along a line parallel to the line connecting the two sources as shown in figure 2.5a, we see more clearly the deep amplitude null, and 180° phase shift. Similarly, if a detector is placed equidistant from the two spatially separated sources, and an object is scanned as shown in figure 2.5b, we see a similar amplitude null and 180° phase shift. One of the exciting effects of the phased array is that when the detector is on the null line, there is no signal from the homogeneous medium. This means that any detected signal is solely due to the presence of a heterogeneity. Such a device is a simple detector for heterogeneities, such as tumors, in highly scattering media such as the breast. We will use this phenomenon to eliminate the background signal when we image heterogeneous media (chapter 4).

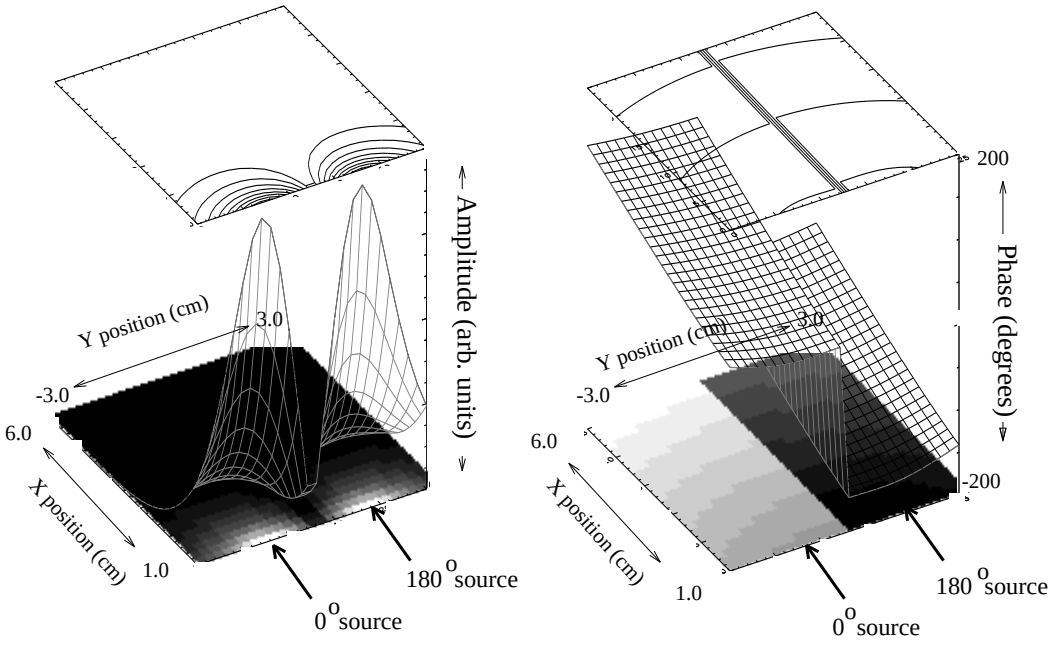

Figure 2.4: The amplitude and phase of a simulated phased array

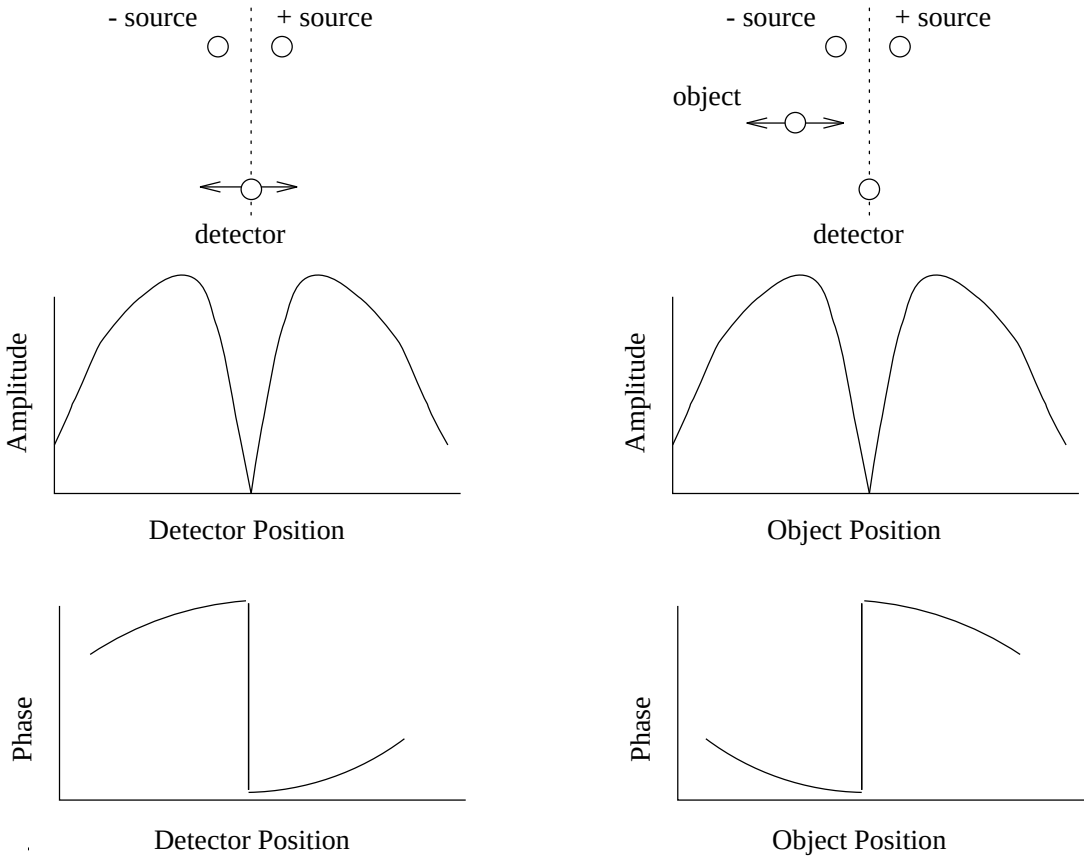

Figure 2.5: The left set of figures shows the measured amplitude and phase as the detector is scanned across the null line and the sources are held still. The right drawings demonstrate the effect of an object which is scanned across the null line. This is equivalent to holding the object fixed and scanning the sources and detector in tandem.

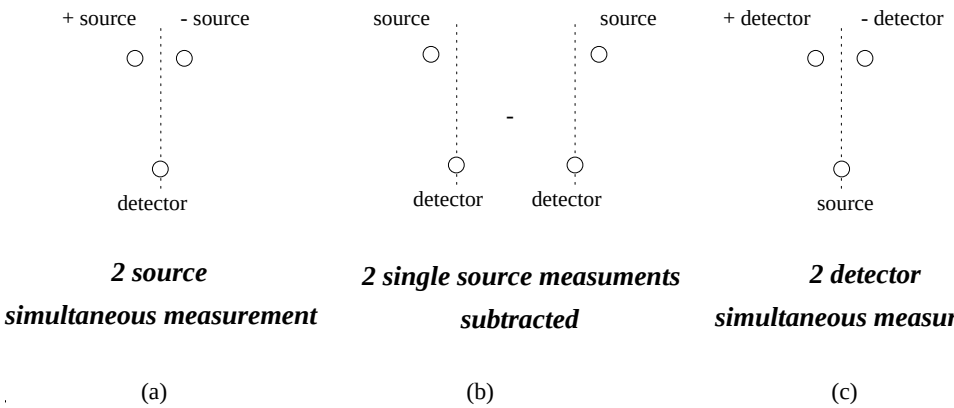

Figure 2.6: Three possible configurations for the phased array measurements.

There are several ways to achieve this superposition of two waves. In the previous discussion, we used two sources, on simultaneously, 180° out of phase (figure 2.6a). We also could use one source, make two separate measurements in the two positions, and subtract the two measurements (figure 2.6b). Similarly, we could use one source and two detectors. There are subtle differences between subtracting two measurements and making one simultaneous measurement of two interfering sources. In the two source simultaneous measurement, the sources must be carefully balanced in amplitude and exactly 180° out of phase. This balance is difficult given variations in individual laser diodes, and the difficulty increases as the modulation frequency increases. In the second configuration (b), the source strength and phase can be calibrated and then incorporated into the subtraction. However, this method will not work if the system changes in the time between obtaining the left and right measurements. The setup shown in panel (c) allows simultaneous dual measurements. The disadvantage of this system is that two parallel detection systems must be built. In our studies we have generally used the configuration shown in (b).

The experiments depicted in this section indicate that it is possible to exert substantial control over the transport of diffuse light in dense random media. We have clearly demonstrated that the index of refraction of these waves depends on the photon diffusion coefficient or random walk step in these media.